Supplementary information for:

Electromagnetic Torque Tweezers: A Versatile Approach for Measurement of Single-Molecule Twist and Torque

Xander J.A. Janssen[1†], Jan Lipfert[1†], Tessa Jager[1], Renier Daudey[1], Jaap Beekman[1], and Nynke H. Dekker[1]

[1]Department of Bionanoscience, Kavli Institute of Nanoscience, Delft University of Technology, Lorentzweg 1, 2628 CJ Delft, The Netherlands
† equal contribution

Consisting of Supplementary Text and 12 Supplementary Figures

Supplementary Text:

Electromagnetic torque tweezers experimental configuration

In the eMTT, electromagnets are combined with a permanent magnet assembly. The permanent magnet assembly consists of a stack of three individual cylindrical magnets with a thickness of 2 mm, an outer diameter of 6 mm, and a cylindrical aperture of either 2 mm (R-06-02-02-G, Supermagnete) or 1 mm (custom part, Supermagnete). Depending on the experiment, we use three different stack configurations i.e. two standard stacks[1] with respectively a 1 mm and 2 mm cylindrical aperture and a third stack with a 2 mm cylindrical aperture of which the bottom magnet is stacked with opposite magnetization direction. This "flipped" geometry[2] gives rise to higher gradient forces compared to the standard cylindrical magnet. The magnet assembly is attached to a translation stage (M-126 PD2, Physik Instrumente) to translate it vertically in order to vary the applied force. The arm holding the translation stage and permanent magnet assembly is mounted onto a manual *xy*-stage (9064-XY, Newport) to facilitate alignment of the magnet assembly in the horizontal (*x,y*)-plane.

The electromagnet configuration consists of two pairs of custom-built Helmholtz coils made from PMMA spools that hold coils of enamel-insulated copper wire (1.5 mm diameter) in place. To yield fields of up to several mT, care was taken to design the coil configuration as compactly as possible, while enclosing a flow cell that uses standard 24 x 60 mm microscope cover slips for experimental convenience. The larger *x*-coils (150 mm diameter, 110 windings) enclose the smaller *y*-coils (100 mm diameter, 100 windings). Within one pair of Helmholtz coils, the two coils are linked in series to supply them with equal currents. The currents through the coil pairs are applied by two power supplies (BOP 36-12D and BOP 20-20D, Kepco) capable of supplying 12 and 20 Amperes, respectively. These power supplies are operated in "voltage-controlled

current-sources"-mode so that the supplied currents, and hence the magnetic fields, remain independent of the coil resistance which may vary due to resistive heating. The voltages that control the power supplies are generated using a DAQ/Amplifier card (M2i.6012, Spectrum Systementwicklung Microelectronic GmbH). By applying sinusoidal currents that differ in phase by 90 degrees between the two coil pairs, a rotating magnetic field of constant magnitude is applied. To protect the coils from high temperatures due to resistive heating, each pair is fitted with a protection circuit (194883 - 89, Conrad Electronic) that cuts power to the coils above a set temperature of 60 $^{\circ}$C.

The beads in the flow cell are illuminated using a collimated LED (XLamp XR-E Royal Blue, Cree) and imaged using an oil immersion objective (PlanC N 100x/1.25, Olympus) together with a CCD camera (RM-6740 CL, JAI). The objective focus is controlled by a piezo stage (P-726, Physik Instrumente) which is mounted atop a custom-built manual stage. To allow manual in-plane positioning, the flow cell is mounted on a *xy*-stage (9064-XY, New Focus).

DNA tether assembly and buffers

DNA tether construction and flow-cell assembly followed methods previously described[3, 4]. PCR fragments, respectively functionalized with multiple biotin and digoxigenin groups, were ligated to the ends of 7.9 kbp DNA constructs. These constructs were incubated for 30 min with either M270 or MyOne streptavidin-coated superparamagnetic beads (Invitrogen). Flow cells were constructed from glass microscope cover slips with parafilm spacers in which the bottom slide was coated with nitrocellulose (0.1 % wt/vol in amyl acetate). Prior to measurement, the flow cell was filled with phosphate-buffered saline (PBS, Sigma) buffer, and non-magnetic latex beads (Life Sciences) were incubated to act as reference beads. After flushing out excess reference beads, the flow cell was incubated with 100 µg/ml anti-digoxigenin (Roche) in PBS for 30-60 min. Following passivation of the flow cell with 2 mg/ml bovine serum albumin (BSA, Sigma), the DNA-coated superparamagnetic beads were flushed in and incubated in PBS buffer for 30 min to allow tether formation. In the last step prior to measurement, the flow cell was extensively rinsed to remove all unbound magnetic beads with buffer. Most experiments employed "PBS+" buffer, which is based on PBS buffer (137 mM NaCl, 2.7 mM KCl, 10 mM phosphate buffer, pH 7.4; Sigma) supplemented with 100 µg/ml BSA, 0.1% Tween, and 5 mM sodium azide. Some experiments employed "TE" buffer, consisting of 10 mM Tris-HCl, pH 8.0, and 1 mM EDTA (Sigma) with varying amounts of sodium chloride added.

For experiments that employed our direct angle tracking protocol[5], we employed M270 beads with 1 µm diameter non-magnetic Fluosphere microspheres (Invitrogen) attached as fiducial markers. To attach the fiducial markers, we first assembled tethered magnetic beads in the flow

cell and then incubated a 1000-fold diluted stock of Fluospheres in PBS+ for 30-60 min, and subsequently rinsed extensively with PBS+.

Calculations of fields and forces exerted by the cylindrical magnet

We calculate the magnetic field and forces generated by the permanent magnet used in the eMTT to apply stretching forces to DNA tethers attached to paramagnetic beads. The magnetic field of the cylindrical magnet with a circular aperture is equal to the superposition of the fields of a solid cylindrical magnet of the same diameter and magnetization and a smaller solid cylindrical magnet with the size of the circular aperture and opposite magnetization (Figure S1)[1]. The magnetic field of a permanent magnet can be calculated using the principle of equivalent sources, which states that the field of the magnet can be computed by considering an ensemble of magnetizing currents. For an ideal, homogenously magnetized material, the current loops inside the material are canceled out by adjacent current loops, and hence the magnetization of the magnet is given by a net current along the outer surface[6]. In the case of a cylindrical magnet with central aperture, the two solid cylindrical magnets are described by two current sheets with currents running in opposite directions: one sheet with a radius equal to the outer radius of the magnet, and a second sheet with a radius equal to that of the circular aperture (Figure S1)[1]. To calculate the magnetic field, we treated each of these cylindrical current sheets as a stack of current conducting loops (Figure S1). The field of a circular current with radius R is cylindrical symmetric and the radial B_{radial} and axial B_{axial} components of the magnetic field at a position (r,z) from the centre of the loop are given by[7]:

$$B_{radial}(r,z) = B_r \frac{2z}{r\sqrt{(R+r)^2+z^2}}\left[-K(k) + \frac{R^2+r^2+z^2}{(R-r)^2+z^2}E(k)\right] \quad (1)$$

$$B_{axial}(r,z) = B_r \frac{2}{\sqrt{(R+r)^2+z^2}}\left[K(k) + \frac{R^2-r^2-z^2}{(R-r)^2+z^2}E(k)\right] \quad (2)$$

where B_r is the residual magnetic field and $K(k)$ and $E(k)$ are the complete elliptic integrals of the first and second kind, respectively:

$$K(k) = \int_0^{\pi/2} \frac{d\alpha}{\sqrt{1-k^2 sin^2\alpha}}$$

$$E(k) = \int_0^{2\pi} \sqrt{1-k^2 sin^2\alpha} d\alpha$$

with the argument:

$$k = \sqrt{\frac{4Rr}{(R+r)^2+z^2}}$$

We calculated the magnetic field of two cylindrical magnet configurations, (6 mm outer diameter, 6 mm height and inner diameter respectively 1 mm and 2 mm), using Eqn. 1 and 2 and numerical integration in MATLAB (Figure S2a). For these calculations, each magnet is approximated by a stack of 0.1 mm thick current loops (Figure S1), where we have verified that the calculated field does not change upon increasing/decreasing the thickness of the current loops by a factor of two. As a numerical example, we evaluate the axial and radial field components at 2, 4, and 12 mm from the bottom surface of the cylindrical magnet. The three horizontal lines (blue, red, and green) in Figure S2a designate the paths over which these two field components are evaluated (Figure S2b-d, using the same color code).

Our field calculations show that the axial field component (Figure S2b) is largely independent of the radial distance (Figure S2c), even over a distance of 1 mm (comparable to the radius of the aperture in the magnet). This independence of radial distance implies that the vertical field is constant within the field of view of the microscope objective (typically 60 x 60 μm). In contrast, the radial component of the magnetic field (Figure S2d), which is zero on the symmetry axis of the magnet, depends strongly on both the vertical and radial distance from the magnet.

From the magnetic field *B*, the force *F* experienced by the paramagnetic bead can be calculated using[6]:

$$\vec{F} = -\vec{\nabla}U = \frac{1}{2}\vec{\nabla}\left(\vec{m}\left(\vec{B}\right)\cdot\vec{B}\right) \qquad (3)$$

where *m(B)* is the field induced magnetic moment of the bead that can be approximated by the Langevin function[8]:

$$m(B) = m_{sat}\left(coth(B/B_0) - \frac{1}{B/B_0}\right) \qquad (4)$$

with m_{sat} the saturation magnetization and B_0 the characteristic field[1].

We measured the vertically-directed force exerted on a Dynal M270 bead, tethered to a 7.9 kb DNA molecule, from the Brownian fluctuations of the bead's position[10], for two different magnets: one with a 1 mm diameter circular aperture (Figure S3a, light brown data) and one with a 2 mm diameter circular aperture (Figure S3a, dark brown data). It is found that the measured force (Figure S3a, square symbols) agrees within the experimental error with the force (Figure S3a, solid lines) calculated from the magnetic field gradient in *z*-direction and the bead's magnetization[6].

Consecutively, we measured the extension of the 7.9 kb DNA molecule at various positions of the magnet above the flow cell. The force-distance

relationship (Figure S3a) was then used to convert the magnet position to force. The resulting force-extension curves (Figure S3b) were fit to the wormlike chain model[9], yielding contour length L_c = 2.8 μm and persistence length L_p = 45 nm for both magnet configurations. These values are comparable to those found by other magnetic tweezers experiments[4].

Measurement of the magnetic field of the Helmholtz coils

To characterize the Helmholtz coils, we measured the magnetic fields at the position of the flow cell as a function of the current though the coils (Figure S4a) using a Hall probe (Gauss meter 5180, FW Bell). The magnetic field was measured for each pair of coils individually i.e. while the other set of coils was switched off. We find linear field vs. current relationships with propertionality constants of 1.19 mT/A for the *x*-coils (Figure S3a, black data) and 1.56 mT/A for the *y*-coils (Figure S4a, red data). The difference in proportionality constants can be understood from the coil geometry i.e. the radius of the *x*-coils is larger and the coils are spaced further apart, hence produce a smaller magnetic field for the same current. To apply a rotating field of constant magnitude, the currents in the different coils pairs therefore need to set in a ratio of 1.30, where the *x*-coils carry the larger current to compensate for their larger size.

To test the homogeneity of the Helmholtz field, we measured the field strength as a function of position within the coil pairs. For the *x*-coils, field components were measured by scanning a three-axis magnetic field probe (MFS-3A, Ametes) over the symmetry axis of the coil pair (Figure S4b; *x*-component (parallel to the symmetry axis), black data points; *y*-component (in the horizontal plane perpendicular to the symmetry axis), red data points). The *y*-component, which can be viewed as the stray field of the *x*-coils, is typically one order of magnitude smaller than the component parallel to the axis of the coil pair. The slight decrease in field midway between the coils is caused by the fact that the coils are not in perfect Helmholtz configuration: for practical reasons (e.g. the *y*-coils have to fit in between the *x*-coils), the distance between the coils is slightly larger than the radius of the coils. Note that within a distance of 1 cm from the center of the coils, the field is homogenous within 0.2% and that the field of view of the objective, i.e. the region in which measurements are taken, is even smaller (typically 60 μm x 60 μm). Similar measurements were performed for the *y*-coils, with comparable results i.e. the stray field perpendicular to the coils axis is at least one order of magnitude smaller than the component parallel to the axis.

The experimentally-measured magnetic fields of the Helmholtz coils can be compared to their theoretically-calculated values. The theoretical computation relies on using the Biot-Savart law for a circular current wire and summing over the windings of the coils given their individual parameters (diameter and position with respect to the origin). The solid black line in Figure S4b shows the measured field values co-plotted with

the calculated field values, where the latter have been scaled by a factor of 0.95 (i.e. the measured field equals 95% of the theoretically predicted field). This small deviation can be explained by e.g. the non-ideal packing of the windings or material properties or a small error in the proportionality constant of the Hall probe.

Tracking of bead position and rotation angle

The *x*, *y* and *z* positions of the paramagnetic beads are determined using conventional tracking algorithms based on cross-correlation analysis[5, 10, 11]. To obtain the rotation angle of the bead, two methods are available: direct tracking of the angular orientation using fiducial marker beads[5] or coordinate transformation of the bead's position from *(x,y)* to *(R,θ)* after fitting a circle to the measured *(x,y)* positions to obtain its center[1]. Attaching a marker bead to the magnetic bead, which is necessary for direct angular tracking, adds an additional step to the experimental protocol that reduces the yield of usable tethers, since not all tethers will have an appropriate marker after the marker bead incubation step. Tracking by coordinate transformation avoids these limitations, but breaks down in the limit of small angular distributions, as thermal fluctuations in the *(x,y)*-position place a lower limit on the angular fluctuations detected using this approach. More precisely, fluctuations in the *(x,y)* position result in apparent angular fluctuations after *(x,y)* to *(R,θ)* conversion. To asses how much the crosstalk influences the results of the angular tracking, we performing both direct angle tracking of the fiducial marker and angle tracking by *(x,y)* coordinate transformation on the same dataset for various forces and trap stiffnesses (Figure S8, left panels). We find that with increasing Helmholtz field, the (x,y)-based angle tracking increasingly overestimates the width of the angular fluctuations and consequentially underestimates the trap stiffness (Eqn. 2 of the main text). This underestimation of the trap stiffness is more pronounced and lower stretching forces (Figure S8, right panels).

The trends can be understood from a simple model that can also be used to correct the (x,y)-based angle tracking results. In the absence of any bead rotation about the *z*-axis (i.e. in the limit of a very large angular trap stiffness k_θ), the bead will undergo fluctuations in the x- and y- position that depend only on the stretching force, tether length and temperature and are given by Eqn. 1 of the main text with $\langle\delta r^2\rangle = \langle\delta x^2\rangle = \langle\delta y^2\rangle$. The thermal fluctuations in (*x,y*) give rise to apparent angle fluctuations after conversion to (*r,*θ), even in the absence of any true bead rotation. The variance of the apparent angular fluctuations $\langle\delta\theta^2\rangle_{xy}$ due to fluctuations in the *(x,y)* position is then given by:

$$\langle\delta\theta\rangle_{xy} = \left(arctan\left(\frac{\sqrt{k_B TL/F}}{R_{circle}}\right)\right)^2 \qquad (5)$$

where k_B is Boltzmann's constant, T the temperature, L the force dependent tether length, F the vertical stretching force, and R_{circle} the radius of the measured circular annulus.
To obtain the "true" rotational trap stiffness, one needs to correct the apparent angle fluctuations observed from (x,y)-tracking by subtracting the component $<\delta\theta^2>_{xy}$. The corrected trap stiffness $k_{\theta,corrected}$ is then given by:

$$k_{\theta,corrected} = \frac{k_B T}{\langle \delta\theta^2 \rangle - \langle \delta\theta^2 \rangle_{xy}} \quad (6)$$

where $<\delta\theta^2>$ is variance of the measured angular fluctuations and $<\delta\theta^2>_{xy}$ the theoretically calculated variance of the angular fluctuations (Eqn. 5). For trap stiffnesses up to ~ 500 pN nm / rad, the corrected trap stiffness agrees well with the trap stiffness determined from direct angular tracking using a fiducial marker (Figure S8, right panels). For trap stiffnesses above ~500 pN nm / rad, the correction factor $<\delta\theta^2>_{xy}$ is of the same order of magnitude as the angular variance $<\delta\theta^2>$ determined from (x,y) to (R,θ) conversion, making correction less precise. We note that typical trap stiffness used in torque and twist measurements on DNA range from 0 to ~ 300 pN nm/rad, a range in which tracking of the bead's angular orientation using its (x,y) coordinates gives accurate results.

Model for DNA buckling and supercoiling

There are several models for the response of DNA to applied forces and torques. Here we follow, with some minor modifications, the approach of Seidel and coworkers [12], which in turn is based on earlier modeling work [13, 14, 15, 16]. We note that our main aim in presenting a model for DNA buckling and supercoiling is not to derive a highly quantitative model and to test it extensively against experimental data. Instead, our focus is to show how a relatively simple model with realistic, but approximate, parameters gives rise to the torque overshoot behavior at the buckling transition and agrees with our experimental observations.
Our model treats DNA as an isotropic elastic rod, with contour length L_C, bending stiffness L_p, and torsional persistence length C. Starting with a torsionally relaxed molecule, we assume that the torque increases linearly with the number of added turns N (justified e.g. by the experimental results of Bryant et al. [17]), such that the torsional energy is quadratic in the number of added turns:

$$E_{pre}(N) = \frac{1}{2}\frac{C_s}{L_c}(2\pi)^2 N^2 \quad (7)$$

C_s is the effective torsional stiffness, which is a function of the applied stretching force F. In principle, one can use the model of Moroz and Nelson[13] for the $C_s(F)$ dependence. In our model, we are directly using the experimentally measured values for C_s at given stretching forces F [18]. The torsional energy in Eqn. 7 increases with added turns until it become

energetically favorable for the DNA to buckle and to form a plectonemic superhelix. Following the model of Brutzer *et al.* [12] and of Daniels *et al.* [19], we make the assumption that first loop of the plectoneme, the "end loop", has a different geometry and a different energy contribution compared to all subsequent loops. The energy of the DNA molecule with N_{wr} turns of writhe within the plectoneme is given by

$$E_{post}(N, N_{wr}) = E_1 + E_2(N_{wr} - 1) + \frac{1}{2}\frac{C_s}{L_c}(2\pi)^2(N - N_{wr})^2 \quad (8)$$

Here E_1 is the energy cost of the first loop and E_2 is the energy cost of any additional writhe within the plectoneme. The mean writhe $N_{wr,0}$ for a given number of turns is determined by minimizing Eqn. 7 with respect to N_{wr} which yields $N_{wr,0}$ and the corresponding post buckling energy:

$$N_{wr,0} = N - \frac{E_2}{\frac{C_s}{L_c}(2\pi)^2} \quad (9)$$

$$E_{post,0} = E_1 + E_2\left(N - \frac{1}{2}\frac{E_2}{\frac{C_s}{L_c}(2\pi)^2} - 1\right) \quad (10)$$

The change in energy at the buckling transition is given by E_{post} - E_{pre}. The fractional occupancy of the post buckling state is given by the corresponding Boltzmann factor:

$$p_p = \frac{1}{1+exp\left(\frac{C_s}{L_c}(2\pi)^2(N_b - N)\left(\Delta N_b + \frac{(N-N_b)}{2}\right)/k_BT\right)} \quad (11)$$

Here, N_b is number of turns at which buckling occurs, i.e. the buckling point, the point at which the pre- and post-buckling states are equally populated. ΔN_b is the change in writhe during the buckling transitions; Seidel and coworkers [12] have shown experimentally that in general $\Delta N_b >$ 1. For the post-buckling energy per plectonemic loop E_2 we use expression derived by Marko [16]:

$$E_2 = 2\pi\Gamma_{post} = 2\pi\left(\frac{2P\left(F - \left(\frac{k_BT \cdot F}{L_p}\right)^{1/2}\right)}{1 - \frac{P}{C_s}}\right)^{1/2} \quad (12)$$

where the parameter P is the twist stiffness of the plectoneme and Γ_{post} is the post-buckling torque . In the model, we can either have the energy of the first loop E_1 as a free parameter or equivalently the change in writhe at the buckling transition ΔN_b. The torque $\Gamma(F,N)$ and extension $z(F,N)$ as a function of stretching force F and the number of applied turns N are given by

$$\Gamma(F,N) = \frac{C_s}{L_c} 2\pi\left(N - N_{wr,0} \cdot p_p\right) \tag{13}$$

$$L(F,N) = L_c \cdot z(F,\Gamma) - \left(\Delta L_1 + (N_{wr,0} - 1)\frac{dL}{dN}\right) \cdot p_p \tag{14}$$

where $z(F,\Gamma)$ is the relative extension of the DNA [13], ΔL_1 is the length reduction of the DNA by the formation of the initial loop, and *dL/dN* is the slope of the rotation extension curve after the buckling transition. The relative extension of the DNA pre-buckling is assumed to have the functional form derived by Moroz and Nelson [13, 14]:

$$z(F,\Gamma) = 1 - \frac{1}{2}\left(\frac{L_p \cdot F}{k_B T} - \left(\frac{\Gamma}{2k_B T}\right)^2 - \frac{1}{32}\right)^{-1/2} \tag{15}$$

The DNA length reduction due to the formation of the first loop is approximated by [12]:

$$\Delta L_1 = \left(\frac{k_B T \cdot L_p \cdot z(F,0)}{2F}\right)^{1/2} \tag{16}$$

For the post-buckling slopes of the rotation curves, *dL/dN*, we can in principle use the results of the composite model by Marko[16]; alternatively, this parameter can be obtained from a straight-forward linear fit in the extension vs. rotation curve, which is the approach that we follow. An overview of all parameters used in the model is given in the next section.

Overview of the parameters used in the model for DNA buckling and plectoneme formation

N – the number of applied turns. This parameter is under direct experimental control, determined by the field rotation applied in the Helmholtz coils.

F – the applied stretching force. The stretching force is controlled by the position of the permanent magnet. We determined the applied stretching force for each bead by analysis of the thermal fluctuations, Eqn. 1 in the main text.

Salt concentration – the ionic strength of the buffer. The ionic strength enters only indirectly, though the salt dependence of *Lp, P, Nb, ΔNb*, see below.

k_BT – The absolute temperature multiplied by Boltzmann's constant. For our room temperature measurements k_BT = 4.1 pN·nm.

L_c – the contour length of the DNA. We assume 0.34 nm per basepair (bp), i.e. L_c = 2700 nm for our 7.9 kbp DNA construct.

L_p – the bending persistence length of the DNA. The bending persistence length of DNA is routinely determined from fits of the worm-like chain model to force-extension data [9, 20] and depends on ionic strength [21]. We use values of L_p = 52, 45, and 42 nm at 20, 150, and 550 mM monovalent salt, respectively, to match previously obtained measurements (Supplementary Figure S12a).

P – The plectonemic twist stiffness. This is a fitting parameter to describe the twist stiffness of the plectonemic state [16]. This parameter also depends on salt concentration [22]. We take P = 32, 25, 18 nm· k_BT at 20, 150, and 550 mM monovalent salt concentration, again to match values previously determined from experimental data (Supplementary Figure S12b).

ΔN_b – The change in writhe at the buckling point. This parameter depends on the DNA length and (relatively weakly) on ionic strength of the buffer and the stretching force. It can be fit to experimental data of the buckling transition. Brutzer, *et al.*[12] determined values of 3.4 ± 0.2 for a 10.9 kbp DNA molecule and 1.6 ± 0.1 for a 1.9 kbp DNA molecule in 320 mM monovalent salt at a force of F = 3.0 pN. We take ΔN_b to be = 2, 2.5, and 3 at 20, 150, and 550 mM monovalent salt and stretching forces of 3-4 pN. We note that the overall behavior of the model does not depend strongly on ΔN_b.

C_s – the effective torsional stiffness. The effective torsional stiffness depends on stretching force. The model by Moroz and Nelson provides an analytical expression for the (approximate) force dependence [13, 14]. For simplicity, we use the independently measured effective torsional stiffness at each given stretching force directly[18].

dL/dN – The post buckling slope (in nm/turn). We determine this parameter directly from the extension vs. turns plots by fitting a straight line in the plectonemic region past the buckling point.

N_b – the buckling point, i.e. the number of turns at which the molecule buckles, defined as the point at which the pre- and post-buckling states are equally populated (cf. Eqn. 5). We fit this parameter directly to the experimental data.

Supplementary References

1. *Lipfert, J.; Wiggin, M.; Kerssemakers, J. W.; Pedaci, F.; Dekker, N. H. Nat Commun* ***2011****, 2, 439.*
2. Kauert, D. J.; Kurth, T.; Liedl, T.; Seidel, R. *Nano Lett* **2011,** 11, (12), 5558-63.

3. *Strick, T. R.; Croquette, V.; Bensimon, D. Proc Natl Acad Sci U S A* ***1998****, 95, 10579-10583.*
4. *Lipfert, J.; Koster, D. A.; Vilfan, I. D.; Hage, S.; Dekker, N. H. Methods Mol Biol* ***2009****, 582, 71-89.*
5. *Lipfert, J.; Kerssemakers, J. J.; Rojer, M.; Dekker, N. H. Rev Sci Instrum* ***2011****, 82, 103707.*
6. *Lipfert, J.; Hao, X.; Dekker, N. H. Biophys J* ***2009****, 96, 5040-5049.*
7. Smythe, W. R. Static and Dynamic Electricity. McGraw-Hill, first edition, **1939**.
8. Fonnum, G.; Johansson, C.; Molteberg, A.; Morup, S.; Aksnes, E.; *J. Magn. Magn. Mat.* **2005**, 293, 41-47.
9. Bouchiat, C.; Wang, M. D.; Allemand, J.; Strick, T.; Block, S. M.; Croquette, V. Biophysical Journal ***1999****, 76, 409-413.*
10. Strick, T. R.; Allemand, J. F.; Bensimon, D.; Bensimon, A.; Croquette, V. *Science* **1996**, *271*, 1835-1837.
11. Gosse, C.; Croquette, V. *Biophysical Journal* **2002**, *82*, 3314-3329.
12. Brutzer, H.; Luzzietti, N.; Klaue, D.; Seidel, R. *Biophys J* **2010**, 98, (7), 1267-76.
13. Moroz, J.D.; Nelson, P. *PNAS* **1997**, 94, (26) 14418-14422.
14. Moroz, J.D.; Nelson, P. *Macromolecules* **1998**, 31, (18), 6333-6347
15. Strick, T.; Allemand, J.; Croquette, V.; Bensimon, D. *Prog Biophys Mol Biol* **2000,** 74, (1-2), 115-40.
16. Marko, J. F. *Phys Rev E* **2007,** 76, (2 Pt 1), 021926.
17. Bustamante, C.; Bryant, Z.; Smith, S. B. *Nature* **2003,** 421, (6921), 423-7.
18. *Lipfert, J.; Kerssemakers, J. W.; Jager, T.; Dekker, N. H. Nat Methods* ***2010****, 7, 977-980.*
19. Daniels, B. C.; Forth, S.; Sheinin, M. Y.; Wang, M. D.; Sethna, J. P. *Physical review* **2009,** 80, (4 Pt 1), 040901.
20. Erie, D.A.; Yang, G.L.; Schultz, H.C.; Bustamante, C. *Science* **1994**, 266, 1562-1566.
21. Baumann, C.G.; Smith, S.B.; Bloomfield, V.A.; Bustamante, C. *PNAS* **1997**, 94, (12), 6185-6190.
22. Mosconi, F.; Allemand, J. F.; Bensimon, D.; Croquette, V. *Phys Rev Lett* **2009,** 102, (7), 078301.

Supplementary Figures:

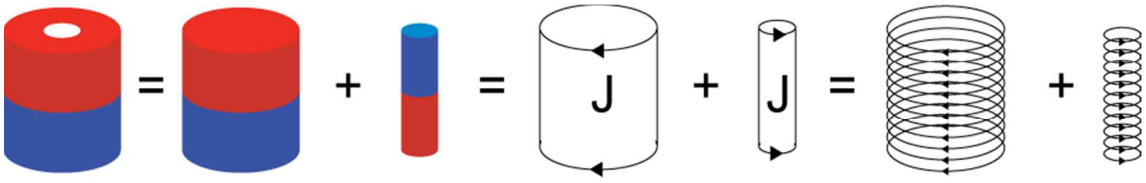

Figure S1: Equivalent currents representing a cylindrical magnet with a circular aperture. For the magnetic field calculations, a cylindrical magnet with a circular aperture can be represented as a superposition of a solid cylindrical magnet of equal size and magnetization and a smaller solid cylindrical magnet with the size of the circular aperture and opposite magnetization[1]. The field of a solid cylindrical magnet with a certain radius, is approximated by the field of a cylindrical sheet (with equal radius) that carries a current density *J*. For the numerical field calculations, the cylindrical current sheets are treated as a stack of 0.1 mm thick circular currents where we have verified that the outcome of the calculations does not change upon increasing/decreasing the thickness of the current loops by a factor of two.

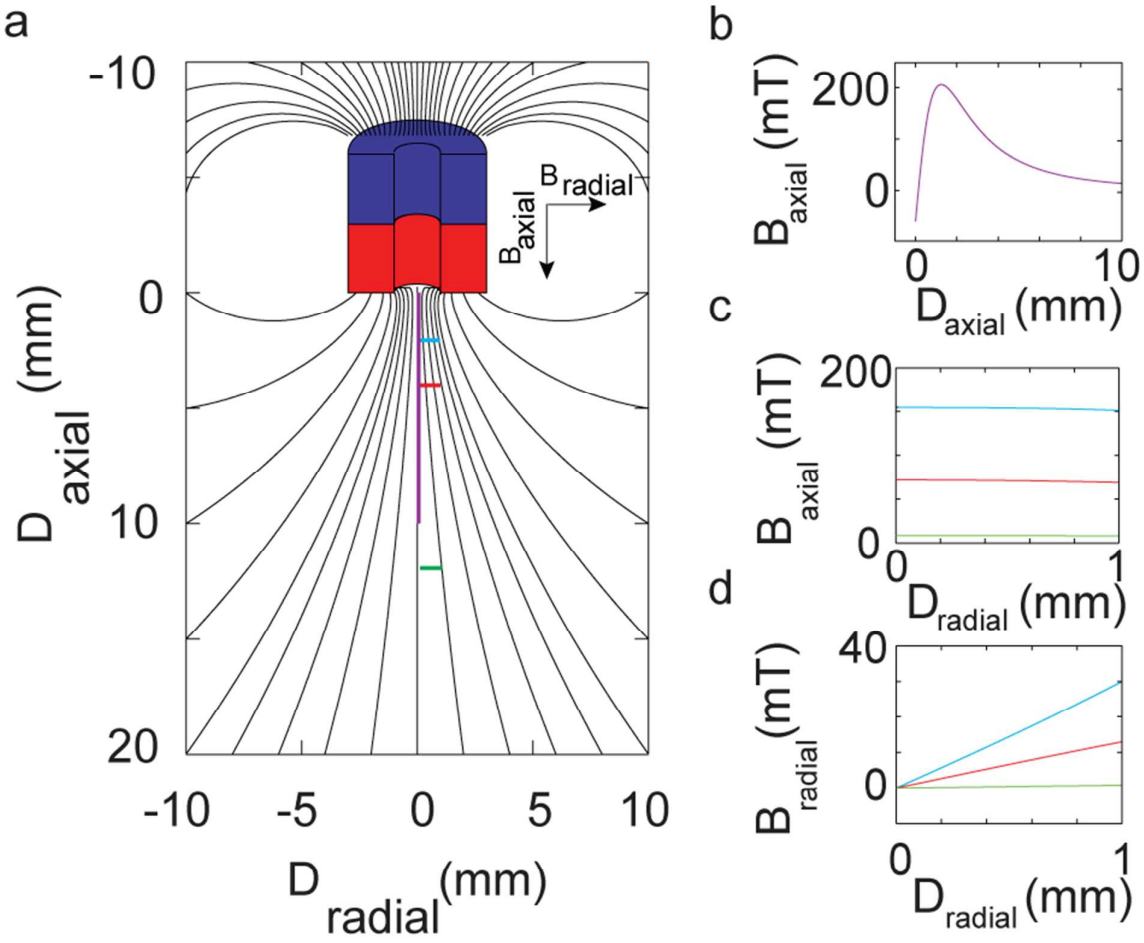

Figure S2: Off- and on-axis fields for a cylindrical magnet. a) Simulation of the magnetic field lines of a cylindrical magnet with an outer diameter of 6 mm, a length of 6 mm and an inner diameter of 2 mm. The purple, blue, red and green lines indicate line traces shown in panels b-d using the corresponding colors. **b)** The axial component of the magnetic field versus the axial distance to the cylindrical magnet along the symmetry axis of the magnet. **c)** The axial component of the magnetic field versus the radial distance calculated at three axial distances (2, 4, and 12 mm) from the bottom edge of the cylindrical magnet. The axial component of the magnetic field changes only slightly with increasing distance from the symmetry axis of the magnet. **d)** The radial component of the magnetic field versus the radial distance calculated at three axial distances (2, 4, and 12 mm) from the bottom edge of the cylindrical magnet. The radial component of the magnetic field increases with increasing distance from the symmetry axis. This effect becomes more pronounced closer to the surface of the magnet. As a result of the radial gradient, the superparamagnetic beads will experience a radially-directed force when positioned off-axis. However, even for M270 beads, the radial forces are in the fN range and negligible compared to the vertically-directed force that is in the pN range.

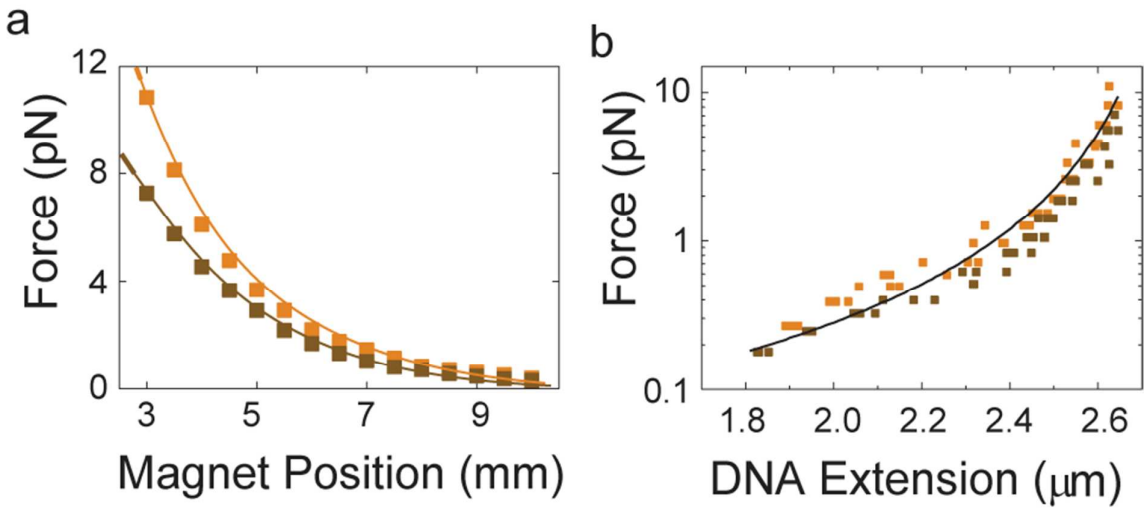

Figure S3: Force-extension measurements on dsDNA using cylindrical magnets. a) The magnetic force on an M-270 bead versus the (axial) distance to the magnet for a magnet with a 1 mm inner diameter (dark brown) and with a 2 mm inner diameter (light brown). Points represent experimental measurements obtained with 7.9 kbp DNA tethers by analyzing the thermal fluctuations (Eqn. 1 in the main text). Solid lines represent the forces calculated from first principles using the magnetic field calculations and taking into account the beads magnetization (Supplementary text on force calculation). **b)** Force-extension curves measured on single 7.9 kb dsDNA tether do not depend on the type of magnet utilized (1 mm inner diameter, dark brown; 2 mm inner diameter, light brown). Values obtained by fitting the worm-like-chain model (solid black line) for the contour length (L_c = 2.8 μm) and persistence length (L_p = 45 nm) are comparable to those found by other magnetic tweezers experiments[6].

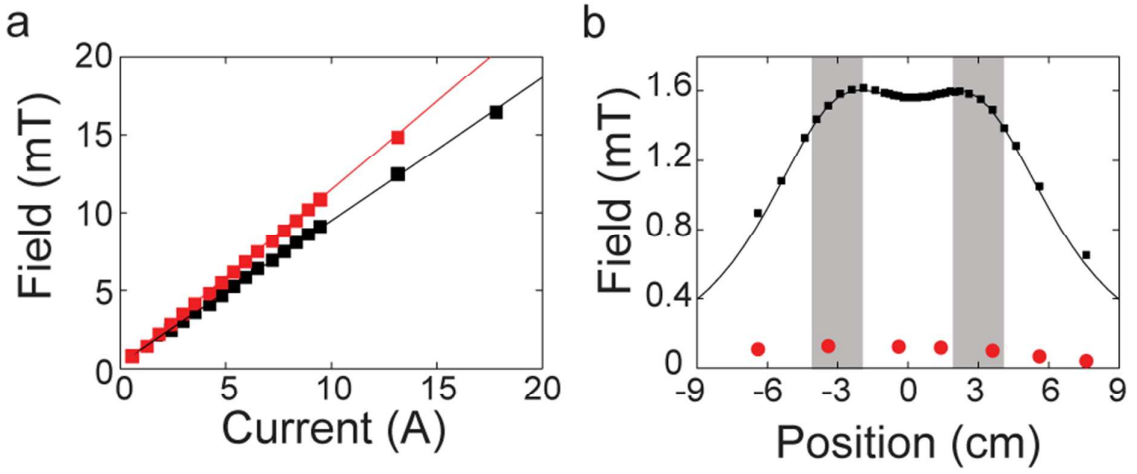

Figure S4: Magnetic fields of the Helmholtz coils a) The amplitude of the axial magnetic field measured at the position of the flow cell center versus the current through the pairs of Helmholtz coils mounted in the x- and y- directions (black and red points, respectively). Due to the different geometries of the two coil pairs, their proportionality constants between field and current differ. The proportionality constants are determined by linear fits through zero (solid lines). **b)** The amplitude of the axial magnetic field as a function of the distance from the midpoint between the Helmholtz coils mounted in the x-direction (black points). The positions of the coils themselves are indicated by the gray shaded areas. The constant field between the coils is indicative of the Helmholtz configuration. The solid line is the magnetic field calculated from first principles fitted to the data using a single multiplication factor, i.e. $B_{measured} = C \cdot B_{theoretical}$ with $C = 0.95$. Also shown is the stray field in the orthogonal direction (red points), which typically amounts to less than 10% of the field amplitude.

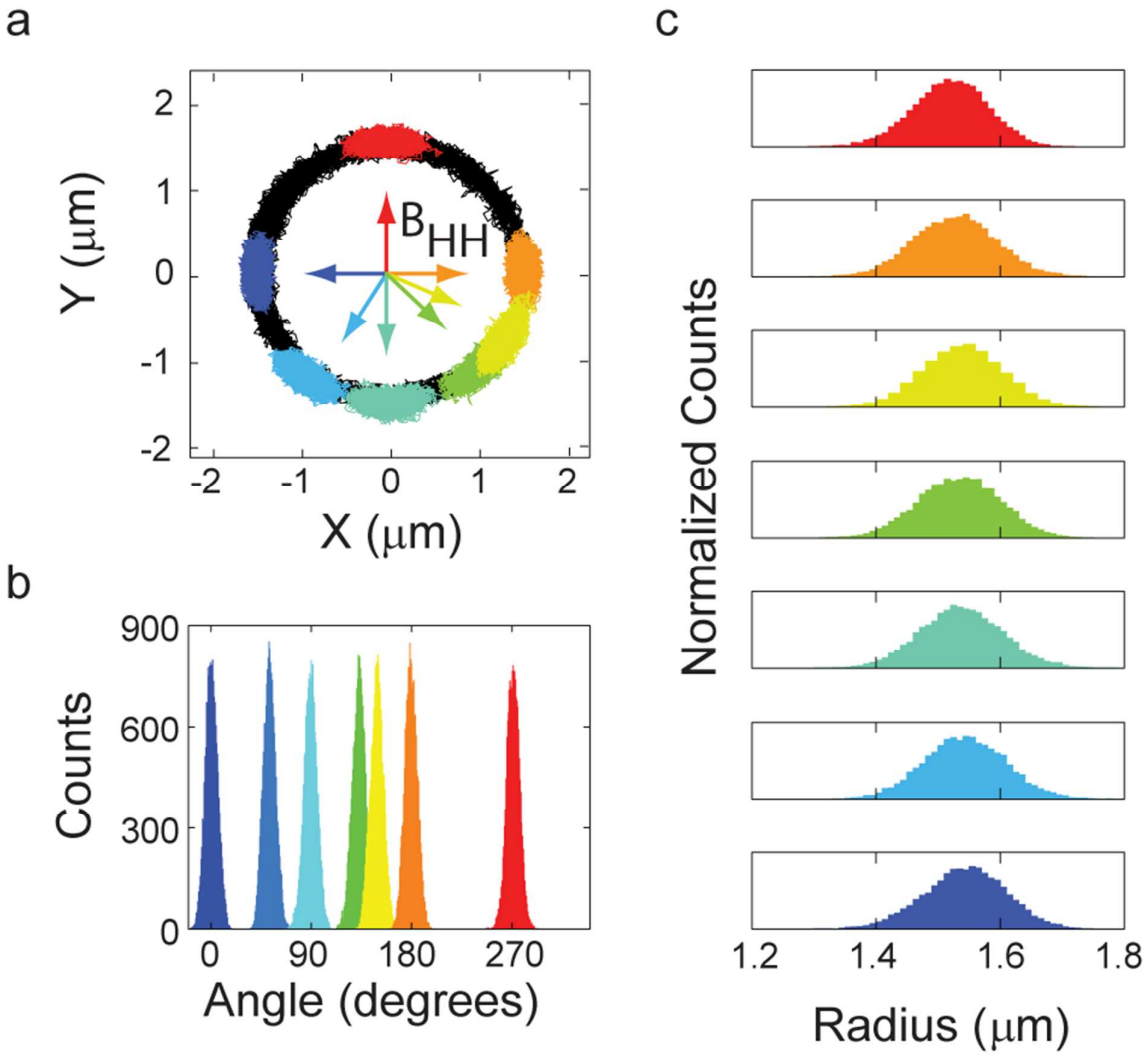

Figure S5: Controlling the rotation of DNA-tethered beads by rotation of the Helmholtz field. a) (*x,y*)-positions of the center of a 2.8 μm diameter bead tethered by a 7.9 kbp DNA construct. In the absence of a Helmholtz field, the bead's center traces out a full circle (black). Applying a Helmholtz field in a given direction (various colors) traps the bead in this direction. **b)** Histograms of the bead's angular orientation after coordinate transformation from (*x,y*) to (*R,θ*). The width of the angle distribution, and therefore the torsional trap stiffness, is independent of the orientation of the torque trap. **c)** Histograms of the radial position of the bead's center after coordinate transformation from (*x,y*) to (*R,θ*). The width of the distribution, i.e. the vertical force, is independent of the orientation of the torque trap. The quantitative analysis and results of this data set are discussed in the main text and plotted in Figure 2.

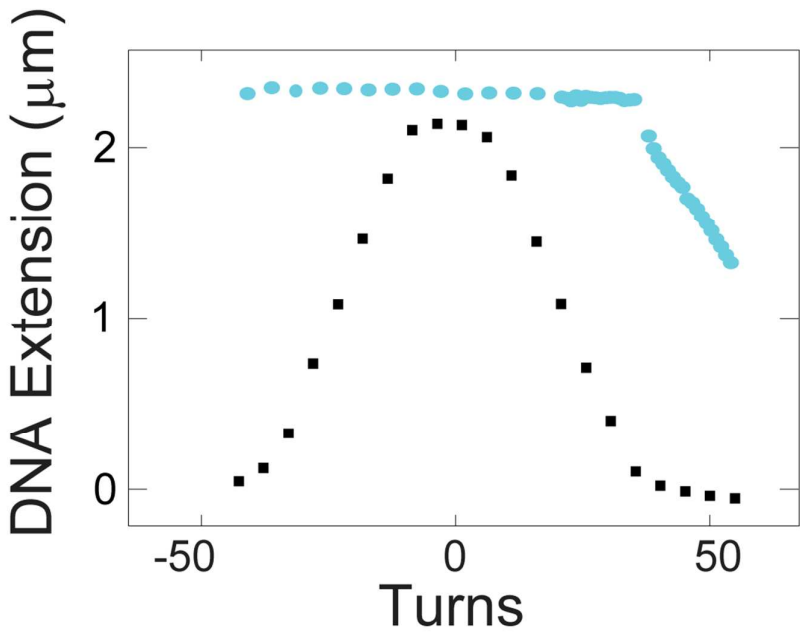

Figure S6: Rotation-extension curves for dsDNA measured in the eMTT. Rotation curves measured using M270 beads and a 7.9 kb dsDNA tether at 0.5 pN (black data) and 4 pN (blue data) display typical behavior upon under- and over-winding of a single rotationally constrained DNA tether [10]. At low forces, the DNA buckles upon over- and under-winding whereas for increased stretching force, the DNA melts upon under-winding.

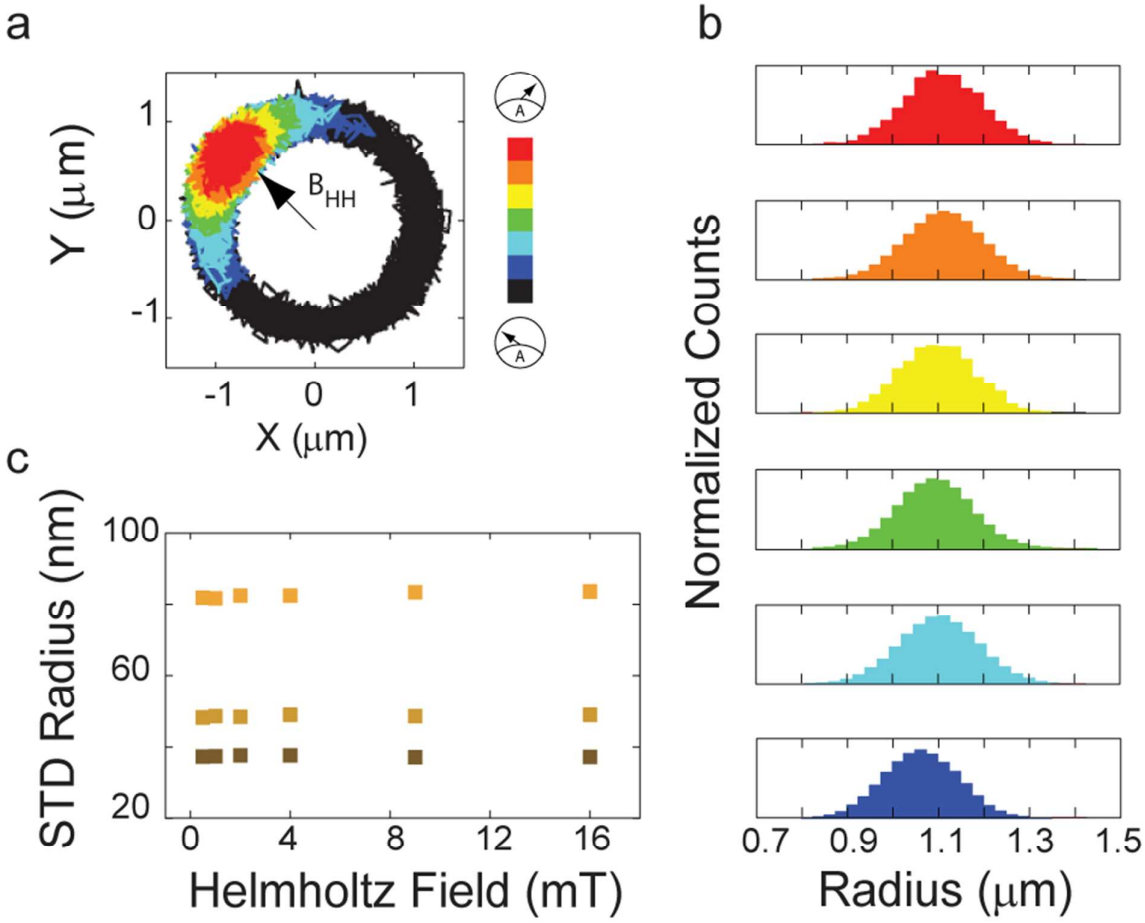

Figure S7: Tunability of torsional trap stiffness by adjusting the amplitude of the Helmholtz field. a) The circular annulus traced out by the bead's center at zero field (black trace) shrinks into progressively shorter arcs with increasing Helmholtz field, indicating increased angular trap stiffness. The value of the applied Helmholtz field is 0, 0.5 1, 2, 4, 8, and 16 mT (shading from black to red). **b)** Histograms of the radial position of the bead's center after coordinate transformation from (x,y) to (R,θ). The width of the distribution, and therefore the vertical force, is independent of the strength of the torque trap. The quantitative analysis and results of this data set are discussed in the main text and plotted in Figure 3. **c)** The standard deviation of the radial distribution decreases with increasing vertical force (1.1 pN, light brown; 3.5 pN, brown; 6.5 pN, dark brown). However, it is independent of the magnitude of the applied Helmholtz field, indicating that the stiffness of the torsional trap can be set independently from the force.

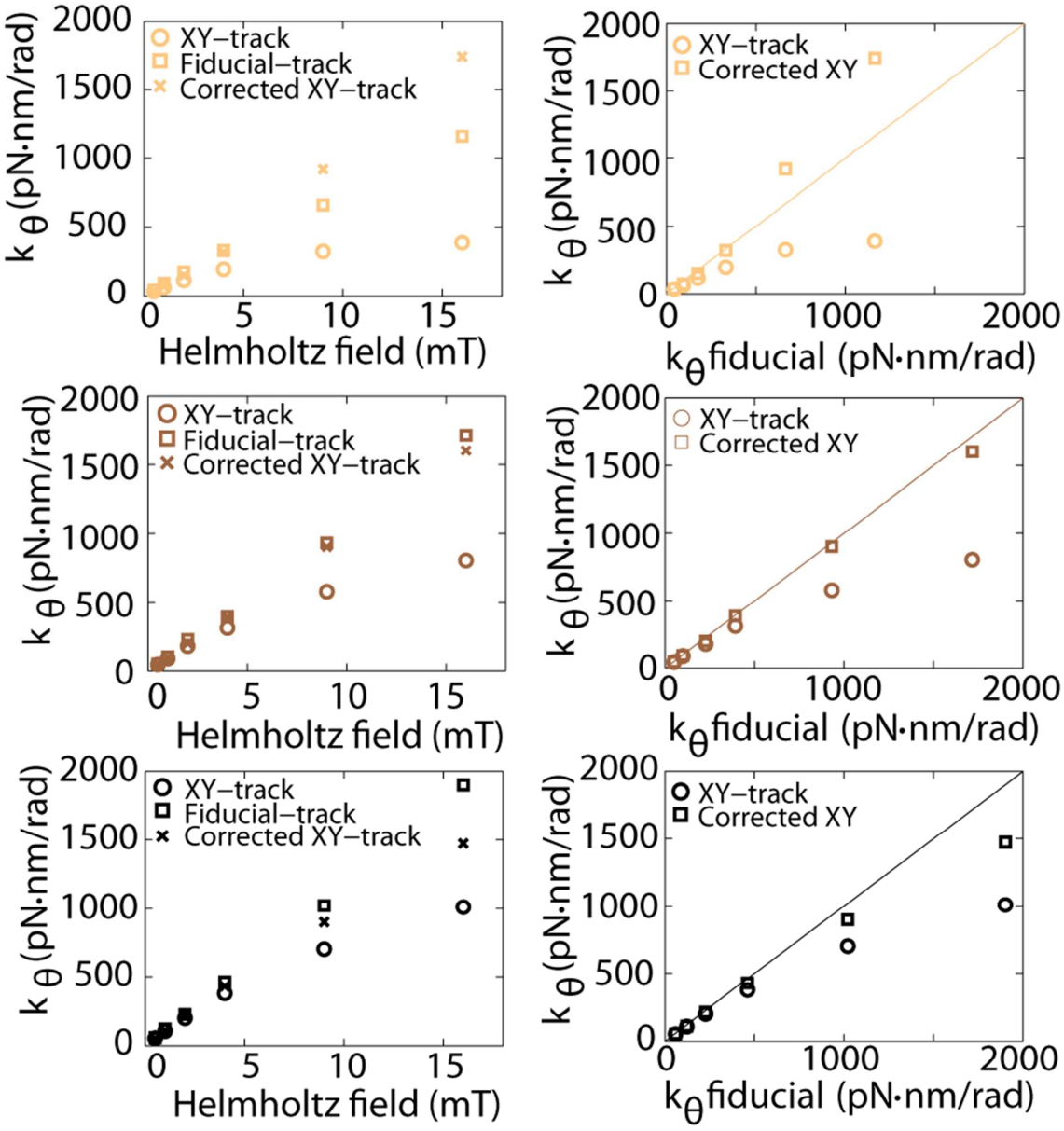

Figure S8: Limitations of tracking rotation angle from the (*x,y*)-position. Performing both direct angle tracking of a fiducial marker and (*x,y*)-tracking on the same data set for various forces (from top to bottom: light brown 1.1 pN, medium brown 3.5 pN and dark brown 6.5 pN) shows an increased underestimation of the measured trap stiffness with increasing applied Helmholtz field i.e. trap stiffness for the (*x,y*) tracking method. For details of the correction procedure, see the section on "Tracking of bead position and rotation angle" above. Correction of the trap stiffness derived from (*x,y*) tracking works up to trap stiffnesses of ~ 1000 pN·nm/rad.

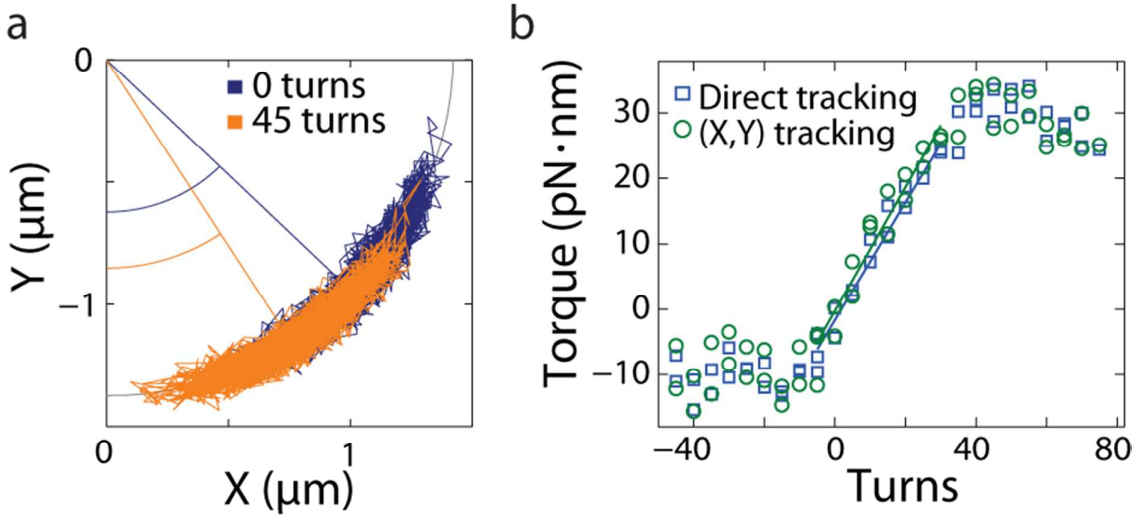

Figure S9: Comparison of direct angle tracking and (*x,y*)-based angle tracking for torque measurements. a) (*x,y*)-positions of a bead tethered to a torsionally relaxed DNA molecule (blue) and after introducing 45 turns (orange). Note that the arc pattern of fluctuations is angularly displaced following the application of 45 turns. The grey line shows the circled fitted to the overall (*x,y*)-fluctuation pattern, determined in a separate experiment. **b)** Applying direct tracking of the fiducial marker (blue squares) and (*x,y*)-tracking (green circles) on the same dataset, yields two torque curves that are identical, within experimental error. Linear fits (solid lines) give a torsional stiffness of 92 ± 11 pN·nm for direct tracking and 90 ± 11 pN·nm for *(x,y)*-tracking.

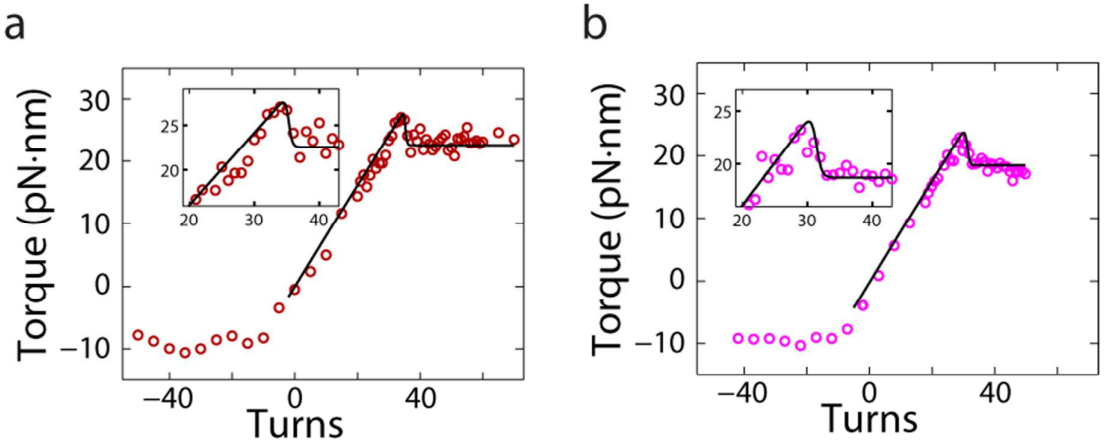

Figure S10: Torque overshoot at the buckling transition. (a) The torque versus number of turns measured in TE buffer + 550 mM NaCl shows a torque overshoot prior to buckling. **(b)** The torque versus number of turns measured in PBS+ buffer supplemented with 400 mM NaCl (550 mM monovalent total) shows a similar trend and a torque overshoot prior to buckling. The solid black lines are generated by our model of DNA buckling and supercoiling, see the section "Model for DNA buckling and supercoiling". Measurements are for 7.9 kbp DNA using 1.0 μm diameter MyOne beads.

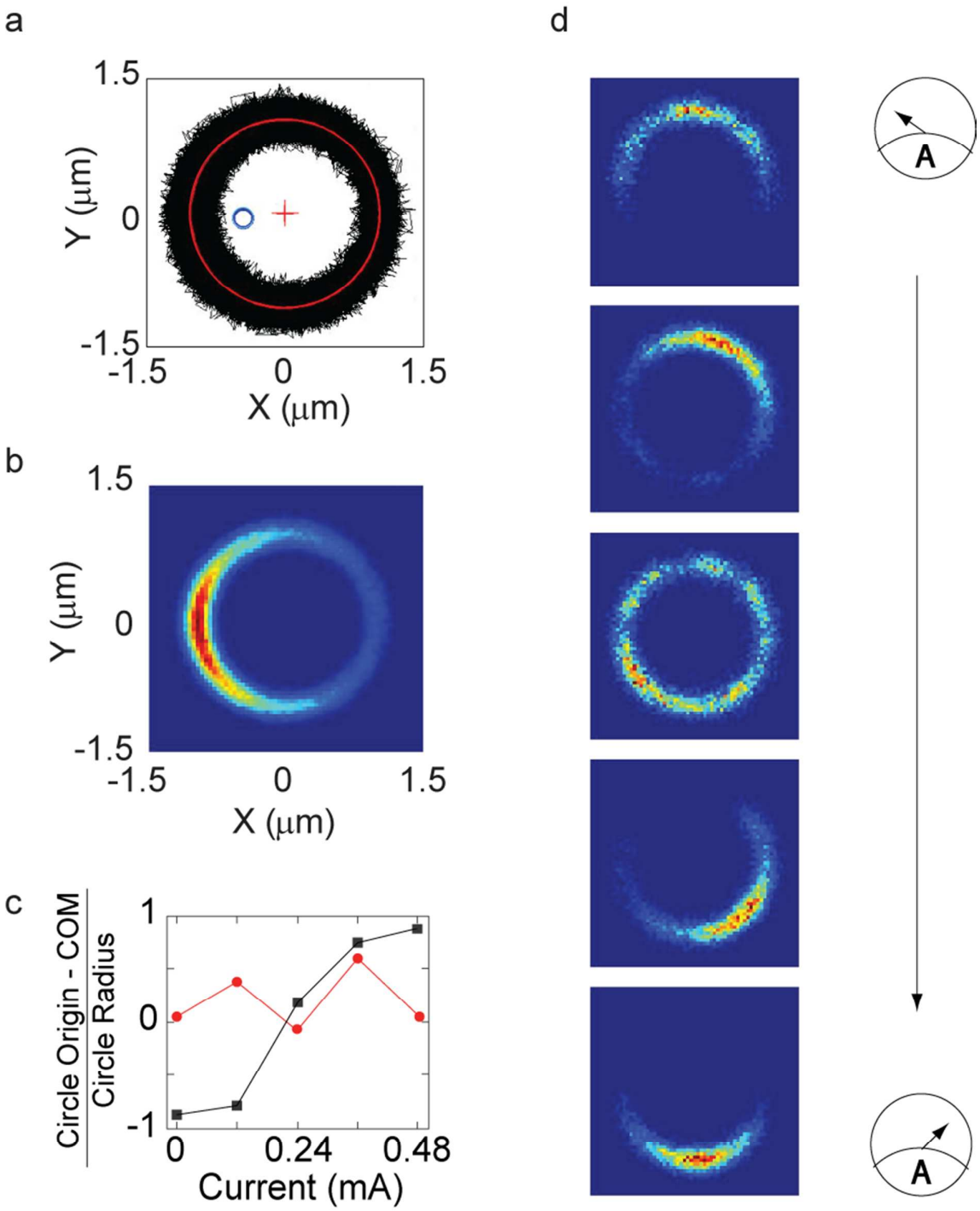

Figure S11: Freely-orbiting magnetic tweezers (FOMT) geometry alignment using electromagnets. a) (*x,y*)-fluctuations of a 2.8 μm diameter M270 bead tethered under a vertical magnet trace out a circular annulus. The red cross indicates the origin of the circle (red line) fit to the data. The center of the circle clearly does not coincide with the center of mass (COM) of the (*x,y*) distribution indicated by the blue circle, indicating that the magnet is not aligned exactly on the bead. The distance between the COM and the circle origin is a measure for the misalignment of the

cylindrical magnet with respect to the bead under investigation. **b)** The thermogram of the (*x,y*)-fluctuation data (color coded from red to blue for high to low occupancy) clearly shows the imbalance in the alignment along the *x*-direction. **c)** Difference between the *x* (black) and *y* (red) coordinates of the COM and those of the circle center normalized on the circle radius versus the current through the coils in *x*-direction. Changing the current through the coils demonstrates the ability to correct imperfections in the circular symmetric potential of the (misaligned) cylindrical magnet. **d)** Thermograms of the (*x,y*)-fluctuation traces measured while increasing the Helmholtz field from 0 mT to 0.48 mT in steps of 0.12 mT. Note that only the *x*-coils are used and that the *y*-coils are switched off.

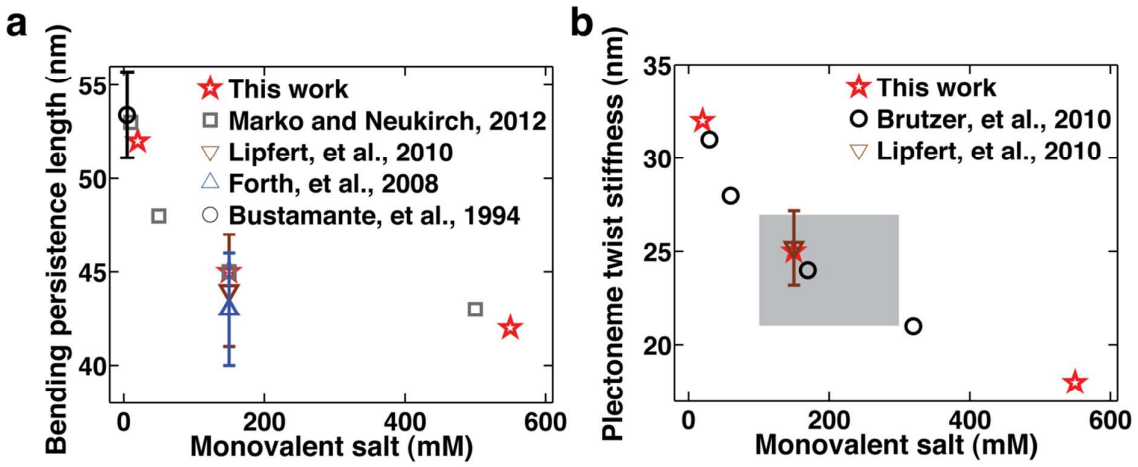

Supplementary Figure S12. Dependence of DNA bending persistence length and plectoneme twist stiffness on monovalent salt concentration. a) Selected literature values of DNA bending persistence length at different concentrations of monovalent salt [18, 19, 20, 23]. The values used in our model of DNA buckling and supercoiling (see the "Model for DNA buckling and supercoiling" section) are shown as red stars. **b)** Selected literature values of the twist stiffness of the plectonemic state as a function of monovalent salt concentration [12, 18]. The shaded grey area denotes the approximate range of values proposed by Marko [16]. The values employed in this work (see the "Model for DNA buckling and supercoiling" section) are shown as red stars.